GFD 2013 Lecture 5: Two-layer bores and non-Boussinesq gravity currents

Paul Linden; notes by Gregory Wagner and Barbara Zemskova

June 21, 2013

1 Introduction

A bore or hydraulic jump is a discontinuity like interfaces which occur between thin, fast moving layers of fluid and thicker, slower moving layers. Bores are commonly observed in everyday life; for example, when a stream of water from a tap strikes a horizontal surface and spreads radially it can be observed to spread at first in a thin layer until some radius at which the thickness of the fluid layer rapidly increases. Such "free-surface" bores also occur in some rivers due to the rising tide, in which case the bore propagates upstream. Two-layer bores are also possible in which a layer of heavy fluid flowing beneath a layer of lighter fluid forms a hydraulic jump; one example of such a bore can be observed over the Cape York peninsula in northern Queensland, Australia, where sea breezes generated off of the Pacific Ocean and the Gulf of Carpinteria collide, giving rise to a bore with a front which, given the correct atmospheric conditions, can form an impressive cylindrical cloud thousands of kilometers long.

Non-Boussinesq gravity currents are common and important: consider a mixture of air and water, whose densities differ by three orders of magnitude. Non-Boussinesq gravity currents exhibit significantly richer phenomena than Boussinesq gravity currents and are not completely understood. In particular, due to the high levels of turbulence associated with the few known experiments, it is unclear whether the current of heavier fluid develops a bore, causing a discontinuous decrease in the height of the layer, or whether the height of the fluid layer increases steadily upstream from the nose of the current.

2 Free-surface bores

A free-surface bore occurs in a layer of fluid flowing over a surface and through some infinite medium which by some mechanism downstream is required to decrease in speed. If the initial velocity of the flow is great enough, a bore will develop involving a sharp increase in the height of the layer and a rapid decrease in its velocity. Figures 1, 2 and 3 show a few examples of bores encountered in rivers, the atmosphere, experiments, and everyday life. In these notes we analyze the two-dimensional case sketched in Figure 4.

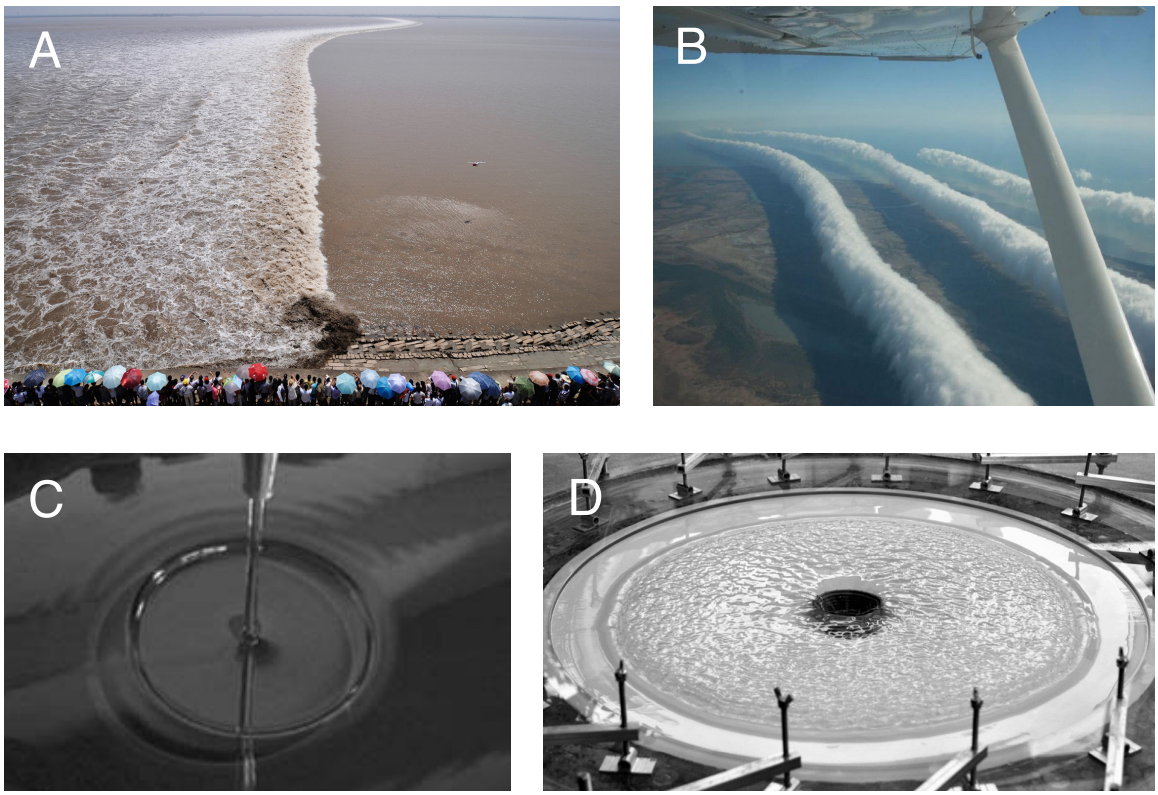

Figure 1: Examples of bores. (A) is a photograph of a tidal bore on Qiantong River in China. The front of the bore is turbulent but it also exhibits waves which can be seen downstream of the front. From `www.theatlantic.com/infocus/2011/10/21st-century-china/100174` (B) is a photograph taken of "Morning Glory" clouds which develop on the crests of an undular bore wave formed by the collision of sea breezes arising on either side of Cape York in northern Queensland. From `www.wikipedia.org/wiki/Morning_Glory_cloud` (C) is an image taken from [3] of a hydraulic jump of the kind observed in everyday life when water falling from a tap strikes a horizontal surface. (D) is an image of an experiment [5] where a hydraulic jump forms due to the radial inflow of water; the experiment is meant to serve as an analog for shocks which form in accretion disks during the formation of a neutron star.

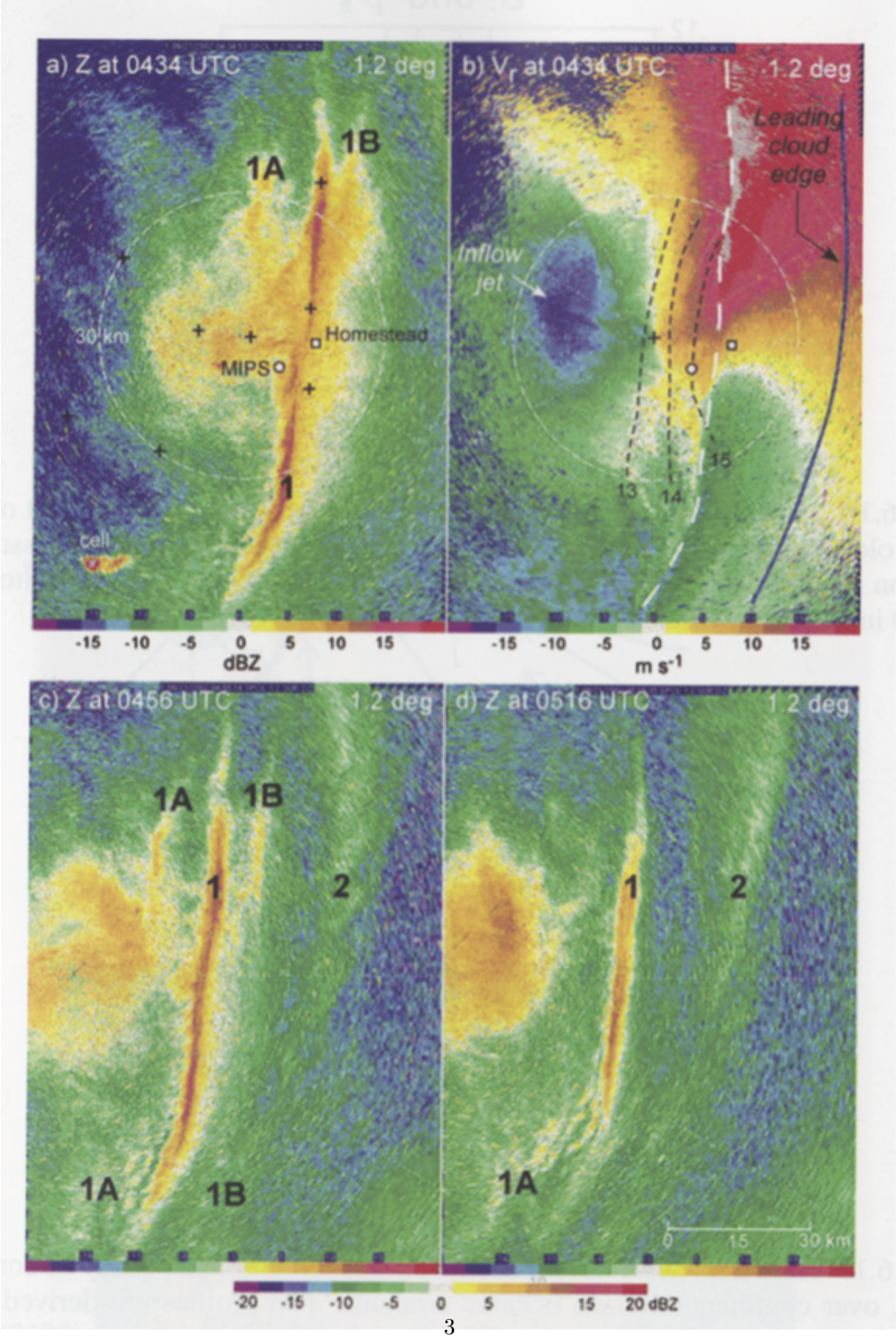

Figure 2: A bore observed in the atmosphere [12]

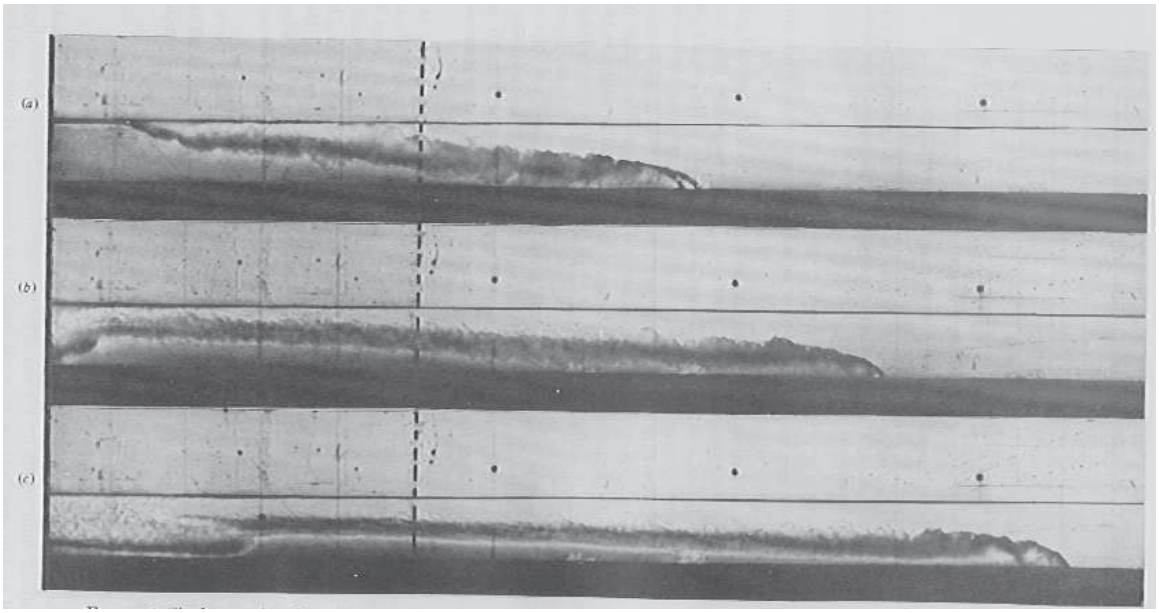

Figure 3: Shadowgraphs of a full-depth lock release. The location of the lock gate is shown by the vertical dotted line. In the top image a light surface current is propagating back into the lock. This reflects from the back wall of the lock and forms a bore, seen as the abrupt change in depth at the rear of the current in the second and third images. While the bore is behind the front, the front travels at a constant speed, as indicated by its position in the second and third images which are taken at equal time intervals. From [10].

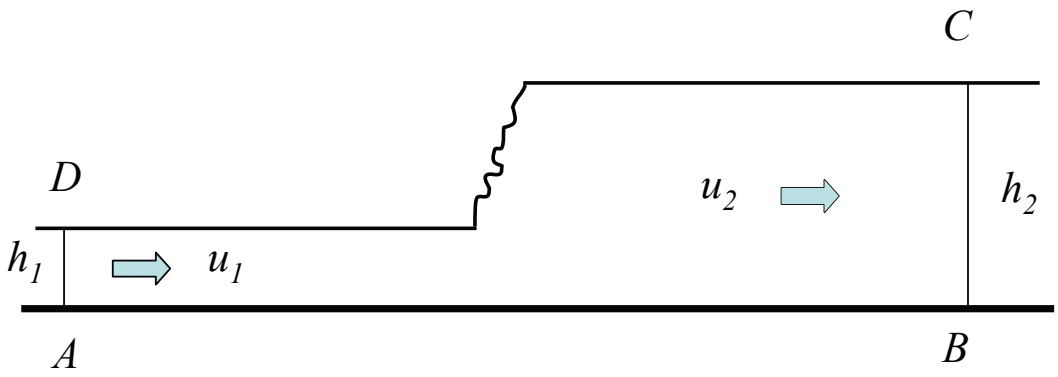

Figure 4: Schematic of a free-surface bore. The control volume affording easy analysis is the rectangle $ABCD$ (where D is properly taken to be at the same height as C). Applying conservation of mass to an accounting of energy flux shows that energy is dissipated only if $h_2 > h_1$. The nature of the front cannot be deduced from this simple analysis; but observations indicate a wave-like front is observed (an "undular bore") while for larger differences the front may become turbulent.

2.1 Analysis

Our approach is to use the same control volume analysis used extensively in the previous four lectures. To the boundaries of this control volume we apply the usual conservation principles for mass and momentum, which are simplified due to the assumption that the flow at each boundary is unidirectional and that pressure is hydrostatic. Conservation of mass implies

$$u_1 h_1 = u_2 h_2. \tag{1}$$

Conservation of momentum requires that the momentum flux, given in this case by

$$\int p + \rho u^2 \, \mathrm{d}z, \tag{2}$$

is equal for the inflow and outflow. If pressure is hydrostatic and given by $p_i = p_{\mathrm{atm}} + g\rho(h_i - z)$, where $i = 1, 2$. Conservation of momentum then implies

$$\frac{1}{2} g h_1 + u_1^2 h_1 = \frac{1}{2} g h_2^2 + u_2^2 h_2. \tag{3}$$

We may confirm the implication of the schematic that $h_2 > h_1$ by calculating the flux of energy through the control volume. The flux of energy through either AB or CD is given by

$$\int up + \frac{1}{2}\rho u^3 + \rho g u z \, \mathrm{d}z, \tag{4}$$

and therefore the flux of energy out of the control volume is

$$\Delta \dot{E} = \rho u_1 h_1 (h_1 - h_2) \left[g + \frac{1}{2} u_1^2 \left(\frac{h_1^2 + h_1 h_2 + h_2^2}{h_2^3} \right) \right]. \tag{5}$$

Therefore we see that because energy can only be removed from the control volume by viscous dissipation or the creation of surface gravity waves, we must have that $h_2 > h_1$. If we insert mass conservation into Equation 3 and solve for u_1 and u_2 we find

$$\begin{aligned} \frac{u_1^2}{g h_1} &= \frac{h_2(h_2 + h_1)}{2h_1^2} > 1, \\ \frac{u_2^2}{g h_2} &= \frac{h_1(h_2 + h_1)}{2h_2^2} < 1, \end{aligned} \tag{6}$$

where the inequalities follow from the fact that $h_2 > h_1$. Taken together these inequalities imply that surface waves generated either in the fluid layer upstream or downstream of the front cannot propagate towards the front, which implies that in the constructed scenario, a sharp continuity or hydraulic jump must exist at the interface between regions 1 and 2.

3 The two layer bore

A two-layer bore occurs when the fluid layer containing the hydraulic jump is overlain by a fluid of different density rather than simply a free surface. The free surface bore is actually a

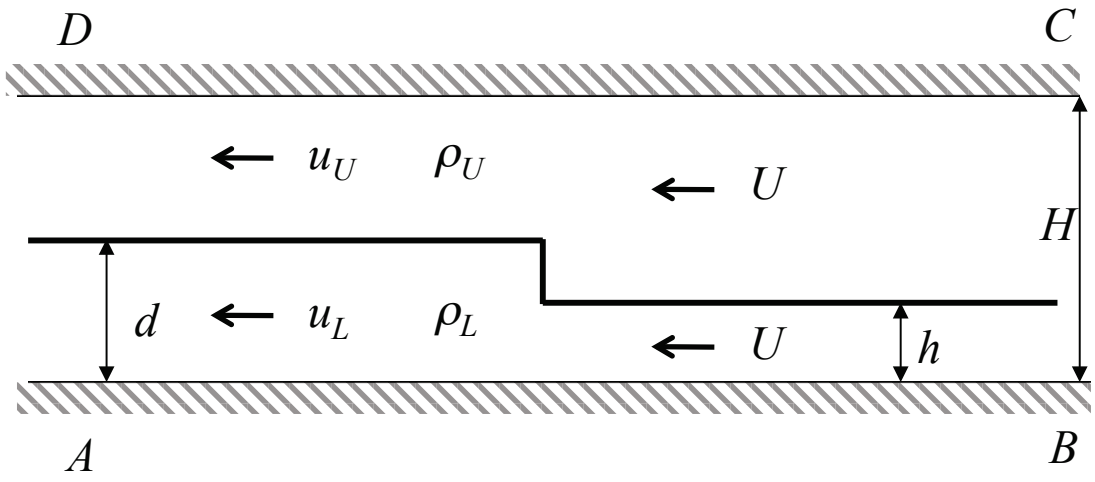

Figure 5: Schematic of a two-layer bore.

subset of this case, corresponding to the limit of vanishing upper layer density. A schematic of the two-dimensional problem is shown in Figure 5.

For the scenario we have two important limits in which we can test our results: the free-surface limit where $\rho_U/\rho_L \to 0$, and the gravity current limit where $h/H \to 0$. In this theory we assume that the flow is uniform, the pressure far from the bore is hydrostatic, and that the two fluids are similar in density such that they satisfy the Boussinesq approximation. The conservation of mass applied to each layer yields two equations,

$$\begin{aligned} u_U(H-d) &= U(H-h), \\ u_L d &= Uh, \end{aligned} \tag{7}$$

and the conservation of momentum along with the assumption that pressure along AB and CD is hydrostatic, yields

$$(p_D - p_C)\,H + \frac{1}{2}g\,(\rho_L - \rho_U)\left(d^2 - h^2\right) = U^2\,(d-h)\left(\rho_L \frac{h}{d} - \rho_U \frac{H-h}{H-d}\right). \tag{8}$$

In this case however we do not have a relation between p_D and p_C as we did in the free surface case when $p_D = p_C$. Because of this we need an additional condition to close the problem. Here we outline three approaches; two which invoke energy conservation in either the upper or lower layer, and a third approach proposed only recently in 2013 which uses a vortex sheet model to estimate vorticity flux of out the domain and thereby form a relation between the difference in velocities and the height of the layers.

3.1 Energy conservation in the upper layer

This approach was considered by Chu and Baddour in 1977 [4] and Wood and Simpson in 1984 [13]. If we presume that energy is conserved in the lighter upper fluid layer, we can alternatively conserve energy flux or apply Bernoulli's theorem between points C and D

(which is less algebraically intensive). Either of these give a relation between p_C and p_D, yielding

$$\frac{U^2}{g'H} = \frac{d(d+h)(H-d)^2}{H^2(2Hh+d^2-3dh)}. \tag{9}$$

Since energy is assumed to be conserved in the upper layer, this solution matches the free-surface solution in the limit $\rho_U \to 0$. However in the gravity current limit when $h/H \to 0$ we find that $U^2/g'H = (H-d)^2/H^2$, which does not match the gravity current solution except in the energy conserving case when $d/H = 1/2$ and $U^2/g'H = 1/4$.

3.2 Energy conservation in the lower layer

Klemp, Rottuno, and Skaworok in 1997 [8] observed that they obtained a closer match to experimental results by conserving energy in the heavier lower layer. Similar to the previous scenario we may either conserve energy flux in the layer or apply Bernouilli along the lower boundary between A and B, yielding

$$\frac{U^2}{g'H} = \frac{2d^2(H-d)^2}{H^2\left(2H(d+h)-2dh\right)}. \tag{10}$$

This solution fails in the free surface limit but produces a better match to experimental results overall.

3.3 Model for vorticity created in mixing layer

A third approach taken by Borden and Meiburg in 2013 [2] is to use the vorticity equation, which eliminates pressure and therefore requires only a model for the vorticity flux in the control volume to form a relationship between the velocities of each layer and their height. The steady, inviscid, 2D vorticity equation can be written

$$\mathbf{u} \cdot \nabla\omega = -g' \frac{\partial \rho^*}{\partial x}, \tag{11}$$

where $g' = g(\rho_U - \rho_L)/\rho_L$ is the reduced gravity and $\rho^* = (\rho - \rho_L)/(\rho_U - \rho_L)$ is a relative non-dimensional density. Integrating over the control volume and applying the divergence theorem yields

$$\oint \omega\,(\mathbf{u}\cdot\mathbf{n})\,\mathrm{d}\ell = -\int g' \frac{\partial \rho^*}{\partial x}\,\mathrm{d}A. \tag{12}$$

If we presume that the density in the control volume is everywhere constant except for a very small region surrounding the front itself, the baroclinic term becomes

$$-\int g' \frac{\partial \rho^*}{\partial x}\,\mathrm{d}A = -g'(d-h). \tag{13}$$

For the integral of vorticity flux over the boundary, we assume that vorticity is zero along the boundary except at the interface between the two fluids downstream of the front. Here we estimate the vorticity with a vortex sheet model such that vorticity is concentrated in a

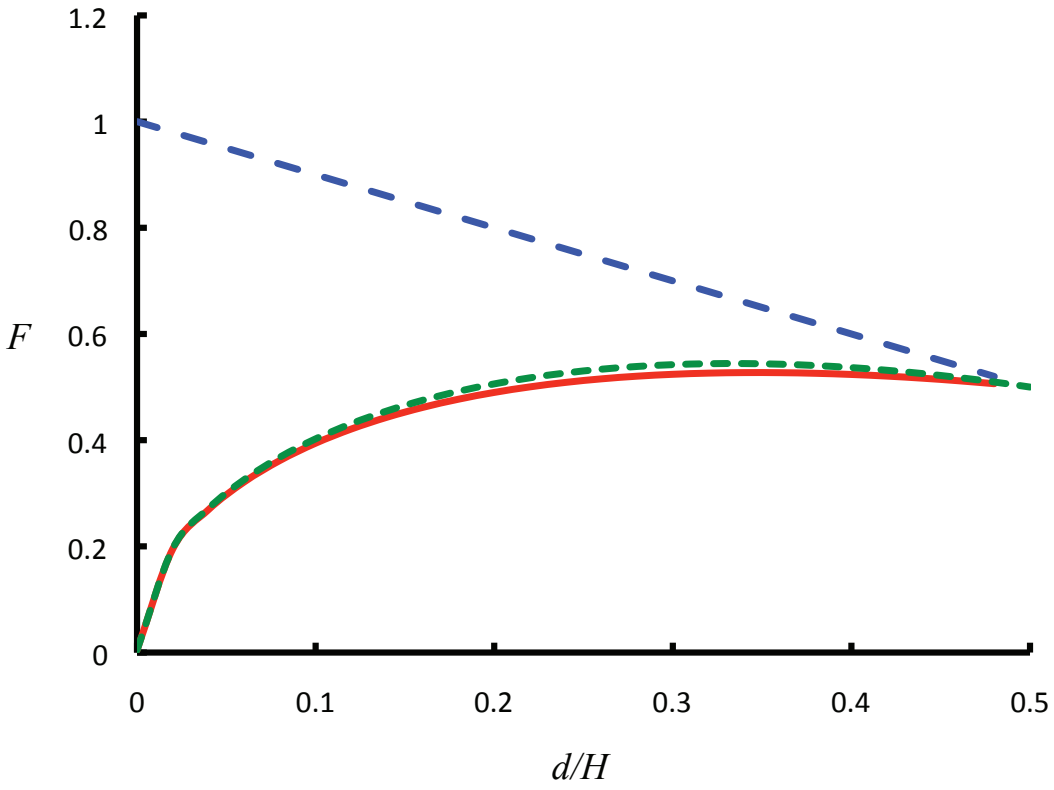

Figure 6: Gravity current speed derived from the limit $h/H \to 0$ for the theories of WS (dashed blue line) [13], KRS (dashed green line) [8] and Borden and Meiburg (solid red line) [2].

thin region on the interface between the two fluids where $\omega = u_U - u_L$ and $u = (u_U + u_L)/2$. These assumptions yield an relation between the velocities of the layers and their heights,

$$\frac{1}{2}\left(u_U^2 - u_L^2\right) = g'\left(d - h\right), \tag{14}$$

which implies

$$\frac{U^2}{g'H} = \frac{2d^2\left(H-d\right)^2}{hH\left(H\left(d+h\right) - 2dh\right)}. \tag{15}$$

It is interesting to note that this solution differs from the solution assuming conservation of energy in the lower, heavier layer only by a factor H/h. The solutions given by the three approaches are compared for the gravity current limit when $h/H \to 0$ in Figure 6, for the speed of the bore as a function of downstream depth d/H in Figure 7, and for the emerged dissipated across the bore in Figure 8.

Additional comparison can be made with two-dimensional numerical simulations carried about by [2]. These results are shown in Figure 9 where the vorticity predicted by a vortex sheet model $\Omega^* = (u_U - u_L)^2/2g'h$ for each method is compared with the vorticity calculated

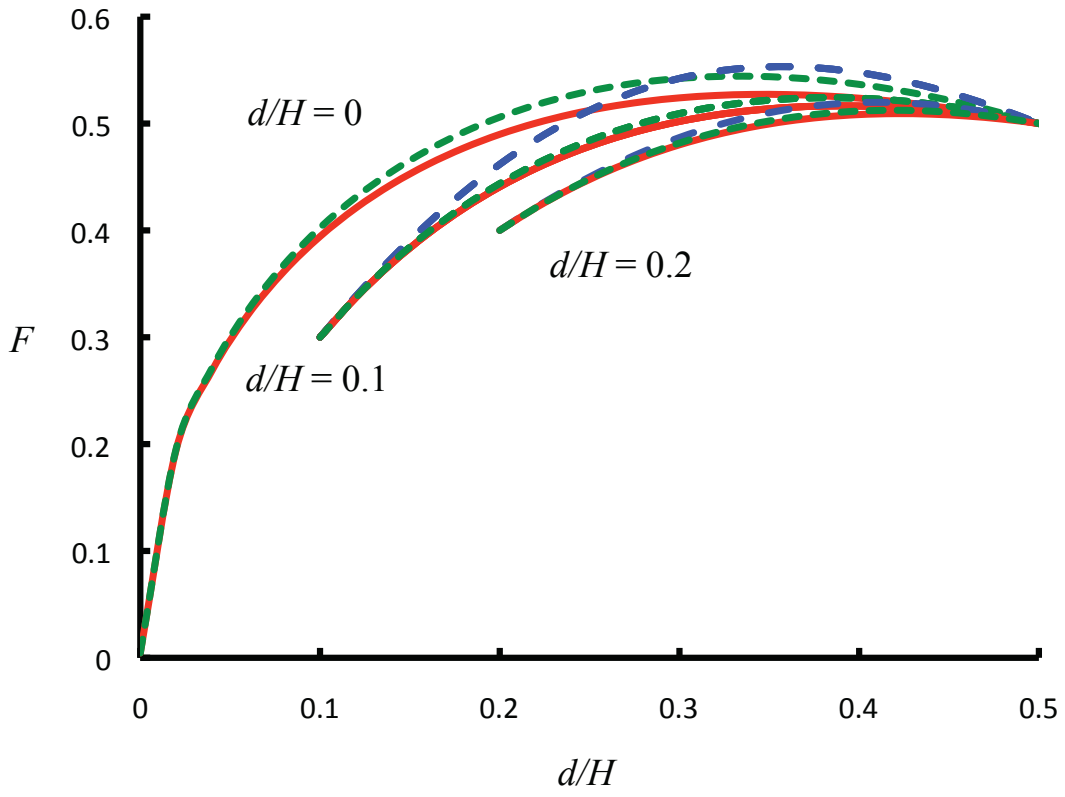

Figure 7: Bore speed as a function of downstream depth d/H for various h/H (erroneously denoted as d/H in center of the figure) for the theories of WS (dashed blue line) [13], KRS (dashed green line) [8] and Borden and Meiburg (solid red line) [2]

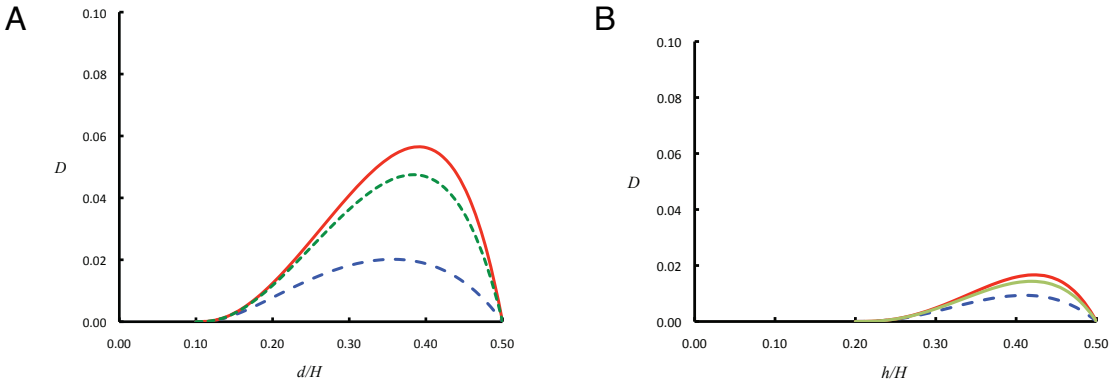

Figure 8: Dissipation across the bore as a function of (A) downstream height d/H and (B) upstream height h/H for the theories of WS (dashed blue line) [13], KRS (dashed green line) [8] and Borden and Meiburg (solid red line) [2].

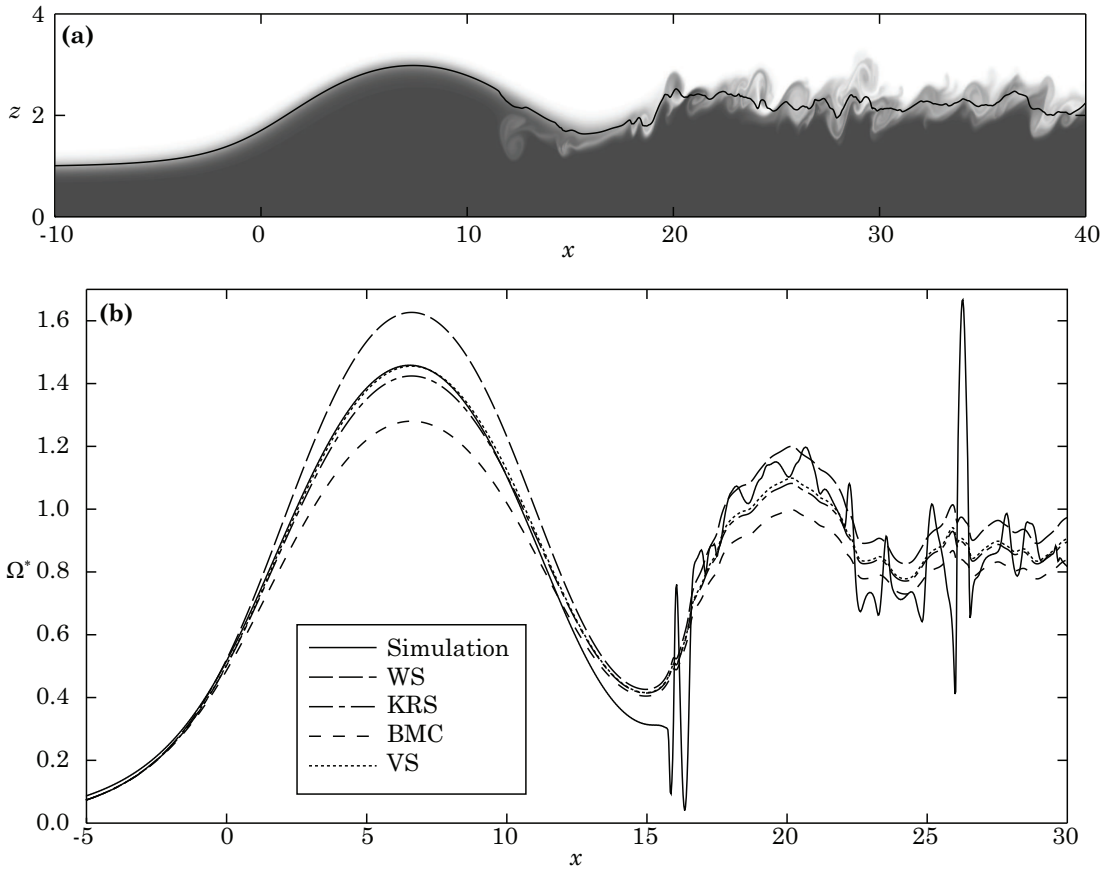

Figure 9: (a) Density field of a DNS simulated bore. (b) A comparison of measured and predicted vorticity from DNS simulations and theories. VS denotes the vortex sheet model proposed by Borden and Meiburg [2]. From [2].

in the simulations. In Figure 10 images taken from a lock exchange experiment are shown; the data from this experiment is shown in Figure 11.

4 Non-Boussinesq Gravity Currents

4.1 Non-Boussinesq Lock Exchange

As we have concluded from Benjamin's theory in Lecture 3, the Froude numbers for heavy and light currents in non-Boussinesq lock exchange are, respectively:

$$F_H = \frac{1}{\gamma} f\left(\frac{h}{H}\right), \tag{16}$$

and

$$F_H = f\left(\frac{h}{H}\right), \tag{17}$$

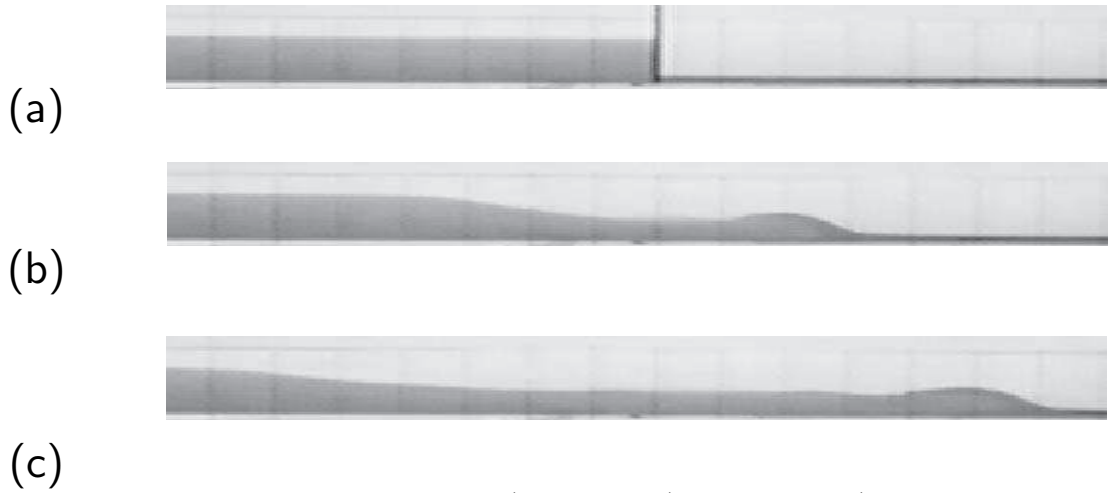

Figure 10: Lock exchange internal bore. (a) initial configuration $t^* = 0$, (b) $t* = 4.6$, and (c) $t^* = 9.5$, where the dimensionless time is $t^* = t\sqrt{H/g'}$. In the initial configuration fractional depths are $D/H = 0.79$ and $L/H = 0.25$. From [11].

where h is the depth of the current, H is the depth of the channel, $\gamma = \rho_U/\rho_L$ is the ratio of densities between the two fluids, and $f(h/H)$ is an unknown function. Since for the non-Boussinesq flows $\gamma < 1$, the heavier fluid travels faster than the lighter fluid. This phenomenon has also been observed in experiments; Figure 12(a) shows the movement of the heavy and light fronts over time after the lock has been removed for an experiment with $\gamma = 0.681$. As time progresses, the heavy front travels further than the lighter front, disturbing the symmetry about the lock observed in Boussinesq lock exchange experiments. This asymmetry becomes even more pronounced as the density difference between the two fluids increases, i.e. γ decreases. The difference in the position of each front relative to the lock is shown in Figure 12(b), with open circles for light front and filled circles for the heavy front. The plots are linear for both heavy and light front, as both are travelling at constant speed (constant velocity phase, see Lecture 2), but the heavier front travels at a greater velocity.

In addition to difference in flow velocities, the light fluid looks more like a Boussinesq flow in an energy conserving case (see Lecture 3): it is more stable and occupies about half of the total channel depth H, while the heavy fluid flow is more unstable and its depth is less uniform, not consistently occupying half of the total channel depth H. This difference is explained through flux imbalance in the schematic in Figure 13. Initially both currents occupy half of the channel depth, and since the heavier fluid is travelling at a greater velocity than the lighter fluid, $Q_1 < Q_2$. In the upper fluid layer, there is a greater supply of the light fluid coming in from the right of the lock than the amount of lighter fluid carried by the light front, creating enough pressure to sustain the upper fluid at half the channel depth. However, for the heavier fluid layer on the bottom, there is an insufficient supply of heavy fluid coming in from the left of the lock compared with the amount carried by the heavy front, so the heavy current eventually cannot be sustained at half the channel depth.

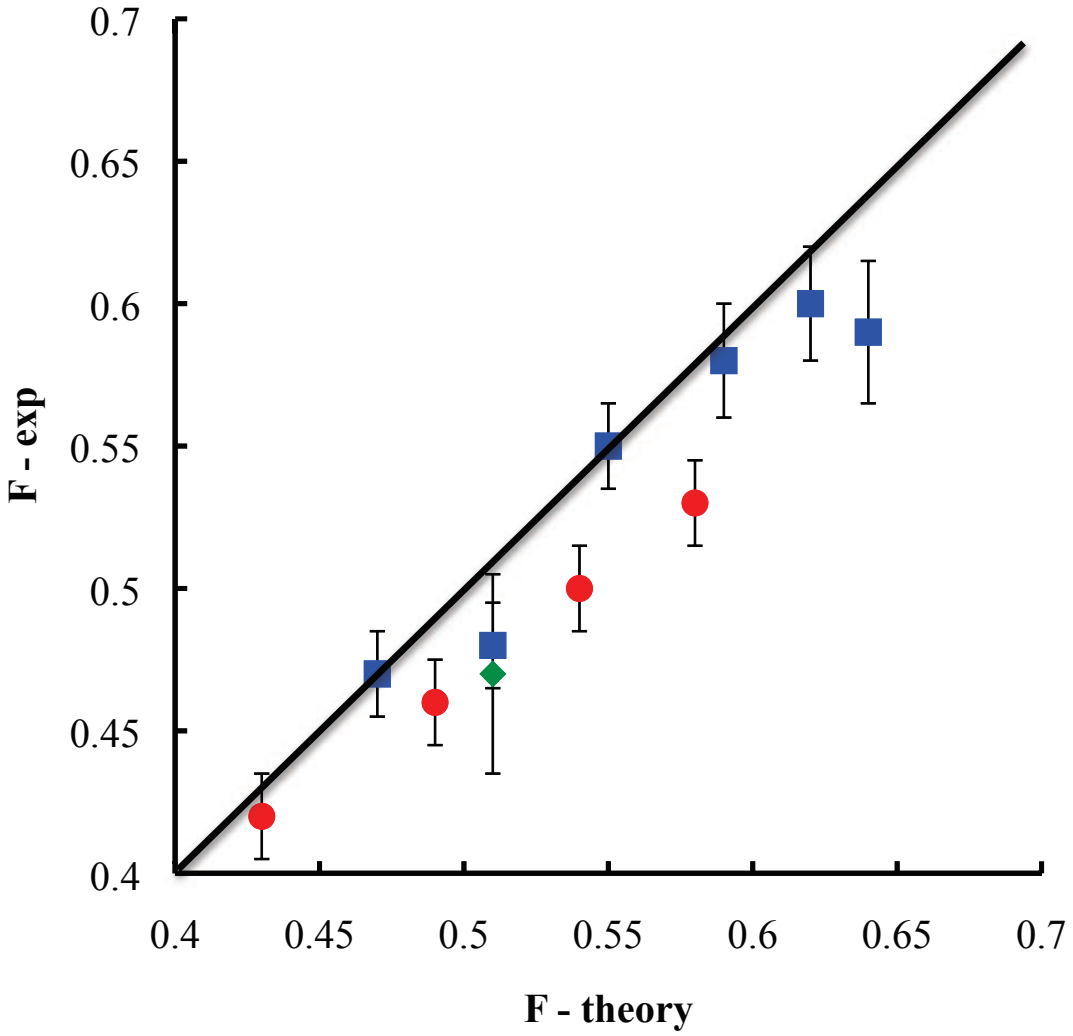

Figure 11: The speed of lock exchange internal bores expressed as Froude numbers. The data are coded according to the depth ahead of the current: squares are for $L/H = 0.1$; circles for $L/H = 0.25$ and diamonds for $L/H = 0.4$. Data from [11].

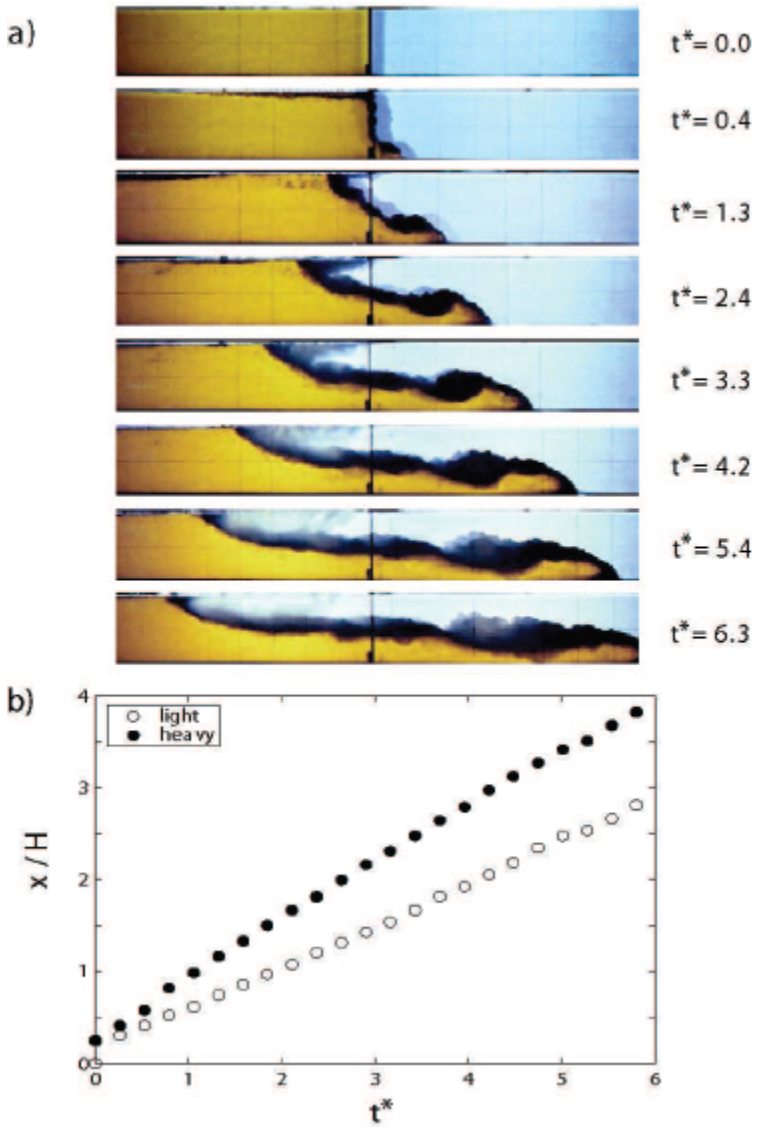

Figure 12: Non-Boussinesq lock exchange with $\gamma = 0.681$. (a) Sequence of shadowgraph images, (b) plot of horizontal position from the lock gate as a function of time; heavy front - filled circles, light front - open circles [9].

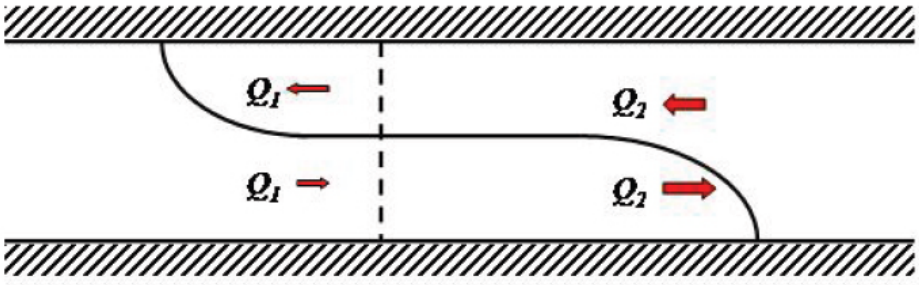

Figure 13: Schematic showing the flux imbalance in a non-Boussinesq lock exchange. $Q_1 < Q_2$ because the heavy current travels faster than the light current, and both currents occupy half the channel depth. As a result, there is enough pressure from the right to sustain the light current at half the channel depth, but not enough pressure to sustain the heavy current at half the channel depth.

4.2 Non-Boussinesq bores and expansion waves

Two possible schematics for non-Boussinesq flows are shown below in Figure (14). In the first scenario (Figure 14(a)), there are two energy-conserving currents that occupy half of channel depth each: left-propagating light current and right-propagating heavy current, which are connected by a long expansion wave and a bore. In the second scenario (Figure 14(b)), the energy-conserving light current, which propagates to the left, is connected by an expansion wave to a shallow dissipative heavy current, which propagates to the right. In Lecture 2, we have seen that a bore can travel faster than the heavy front, so once the bore catches up with the front, the flow schematic results in the second scenario.

The flow depth and the speed of the expansion wave can be obtained using shallow water theory for a 2-layer system by solving the following system of PDEs by the method of characteristics:

$$\begin{aligned} \frac{\partial h_L}{\partial t} + \frac{\partial}{\partial x}(h_L u_L) &= 0, \\ \frac{\partial u_L}{\partial t} + a\frac{\partial u_L}{\partial x} + b\frac{\partial h_L}{\partial x} &= 0, \end{aligned} \tag{18}$$

where $h_L(x,t)$ is the current depth, $u_L(x,t)$ is the current speed, and a is defined

$$a = \frac{u_L(h_U - \gamma h_L) + 2\gamma u_U h_L}{\gamma h_L + h_U}. \tag{19}$$

Figure 15 shows the speed u_L of the expansion wave in the lower fluid layer as a function of h/H for different γ values. As the lower fluid layer occupies closer to half of the channel depth, the velocities of the expansion waves roughly converge. However, as the flow becomes shallower (h/H decreases), the expansion wave travels faster for larger γ values.

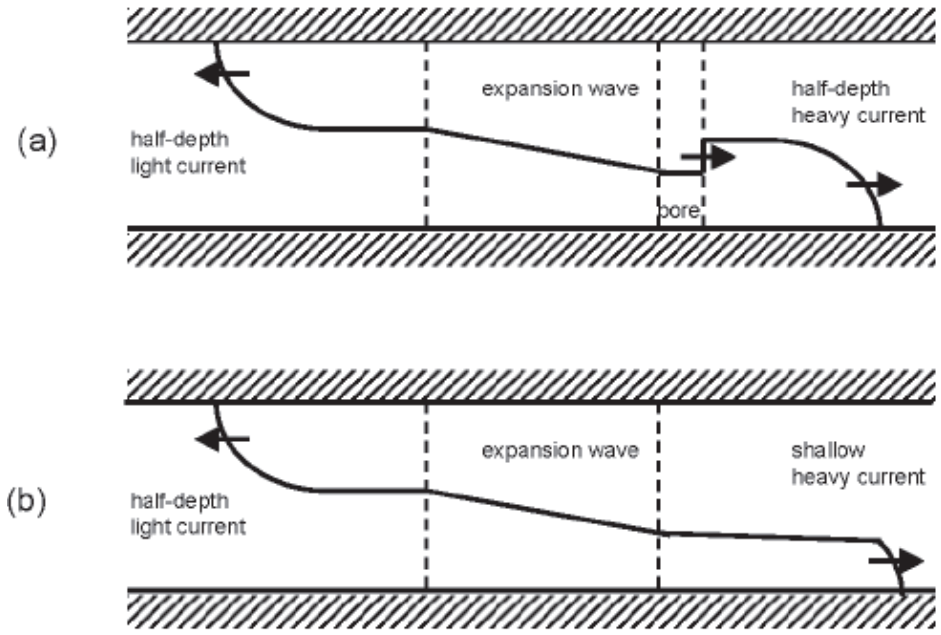

Figure 14: Diagram of two types of lock exchange flows: (a) left propagating energy-conserving light current, and right propagating energy conserving heavy current, connected by a long expansion wave and a bore; (b) left propagating energy-conserving light current, and right propagating dissipative heavy current connected by an expansion wave.

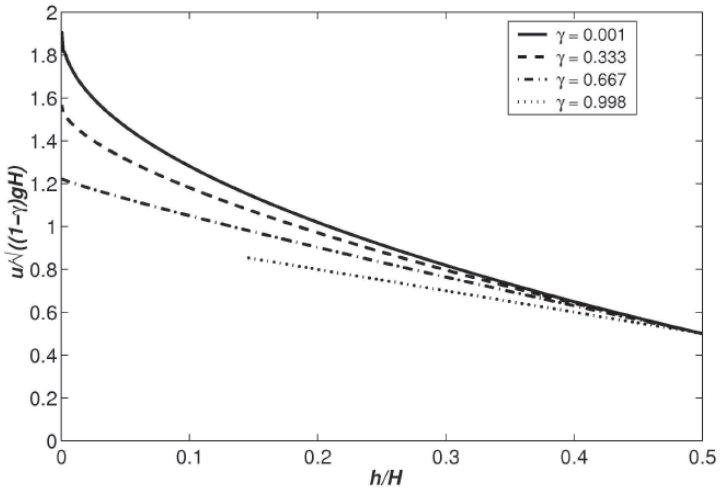

Figure 15: Speed u_L in the lower layer in the expansion wave as a function of lower layer depth h_L for different γ values.

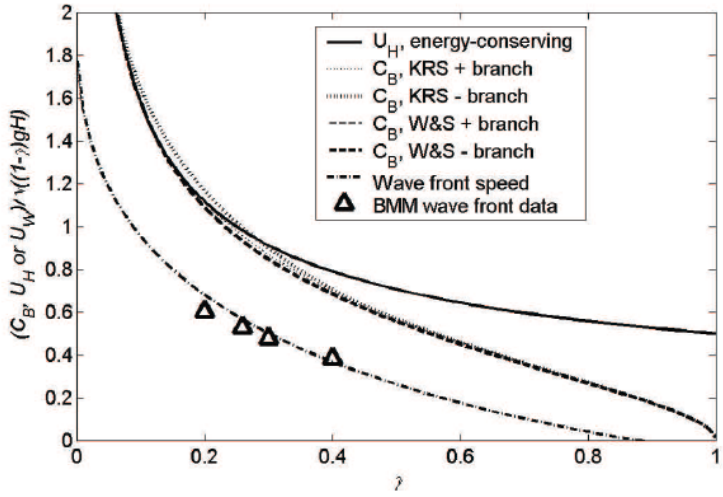

Figure 16: Bore speeds C_B computed using two theories, KRS (dotted lines) [8] and WS (dashed lines) [13] compared with U_H, the energy-conserving heavy gravity current speed (solid line) as a function of γ. The dash-dot line is the theoretical expansion wave front speed, which is lower than the bore speed for all γ values.

Furthermore, the bores speeds can be computed using either the Klemp, Rottuno, and Skamarock (KRS) model [8] or the Wood and Simpson (WS) model [13], both of which are not accurate in certain limits, as discussed in the first part of this lecture. Nonetheless, the bore speeds from these models (4 dashed lines) are compared with the flow velocity of energy-preserving right-propagating heavy front (solid line), and expansion wave velocity (dot-dashed line) for different γ values in Figure 16. This figure shows that for $\gamma > 0.3$, the bore travels slower than the energy-preserving heavy front, thus maintaining the schematic (a) in Figure 14. However, for γ values less than approximately 0.3, the bore velocity from positive branch of the KRS model is greater than the energy-preserving heavy front velocity, and the other bore velocities are very close to the energy-preserving heavy front velocity. Therefore, the bore can potentially travel faster than the heavy front for sufficiently small γ values, so that the flow schematic results in case (b) in Figure 14. Figure 16 also shows that the expansion wave speed is lower than that of a bore and of an energy-preserving heavy front, thus adhering to the schematics in Figure 14.

As for the velocity of the light front, both experimental and numerical results conclude that it travels roughly at the speed of the energy-preserving front, independent of the γ values. These results are shown in Figure 17, where the solid line is the theoretical speed of energy-preserving front, and triangles are numerical simulation results [1], and other markers are experimental results. These results also agree with energy-preserving scenario, since the front height is approximately half of the channel width, as predicted from the theoretical derivations, which is shown in Figure 18.

Unlike the light front, the velocity and the height of the heavy front cannot be predicted by the energy-preserving theory. Figure 19 shows the numerical (triangles) [1] and experi-

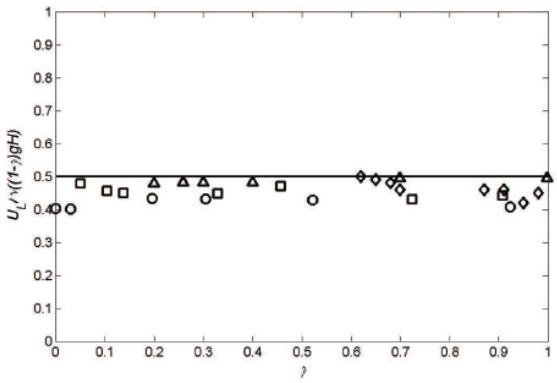

Figure 17: Light current speed: comparison of theoretical front speed (solid line) and numerical [1] and experimental measurements [6, 7] of U_L, as a function o γ.

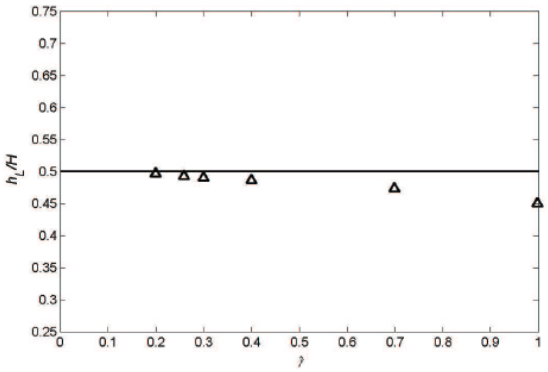

Figure 18: Light current speed: comparison of theoretical front height (solid line) and numerical measurements (triangles) of H_L [1], as a function of γ.

mental (other markers) [9, 6, 7] results for the heavy front velocities for different γ values compared with the energy-preserving front velocities (dashed line), front velocities for KRS bore model [8] (Figure 14(a) scenario, solid line), and front velocities for dissipative gravity current (Figure 14(b) scenario, dotted line). For $\gamma < 0.55$, the heavy front velocities are less than the ones predicted by the energy-preserving theory; and although the other two theories also overestimate the heavy front velocities, they produce better approximations than the energy-preserving theory. This fact is better illustrated in Figure 20, which shows the heavy front heights as a function of γ from the above theories and numerical and experimental results. The front height approaches $H/2$, value predicted by the energy-preserving theory, only when γ is very close to 1 (Boussinesq case). However, for smaller γ values the front height can be fairly well predicted by both the KRS bore theory (solid line) and the dissipative gravity current theory (dotted line), indicating that both configurations in Figure 14 are possible. In reality, in the experimental and numerical work, it is difficult to visually identify the presence of a bore. To illustrate this point, one can compare the outlines of a theoretical shape of the flow with a bore (top) and without a bore (bottom) overlaid on top of an outline (dotted) of the computed gravity current for $\gamma = 0.7$ in Figure 21.

4.3 Stability of non-Boussinesq gravity current

Using the linear stability theory, we can also calculate the wave number k for the interface between the heavy and the light gravity currents by solving:

$$\frac{\partial^2 \phi_i}{\partial x^2} + \frac{\partial^2 \phi_i}{\partial z^2} = 0, \tag{20}$$

where $i = 1$ for the upper lighter layer and $i = 2$ for the lower heavier layer, and the interface can be expressed as:

$$\phi = \hat{\phi}(z) e^{ik(x-ct)}. \tag{21}$$

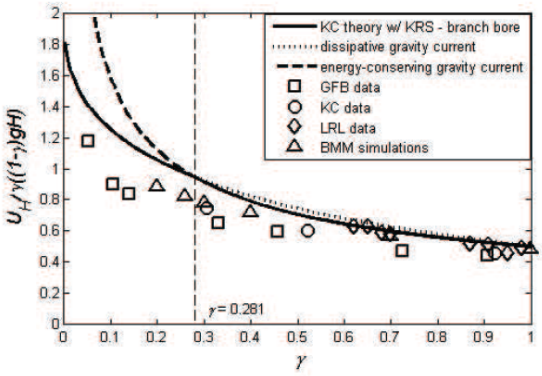

Figure 19: Heavy current speed: comparison of theoretical front speed (solid line) and numerical [1] and experimental [9, 6, 7] measurements of U_H, as a function o γ.Energy-conserving case is plotted as a line, bore-configuration theory is solid line [8], and dissipative gravity current (without a bore) is a dotted line.

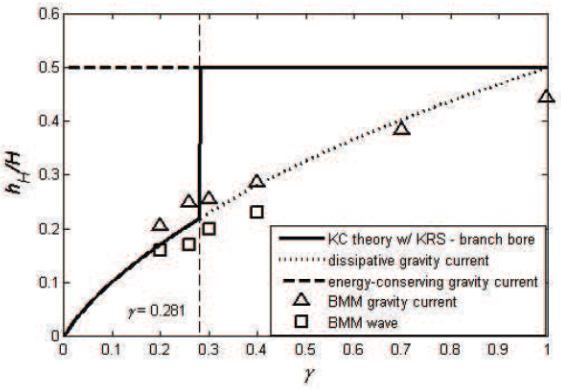

Figure 20: Heavy current speed: comparison of theoretical front height (solid line) and numerical measurements (triangles) of H_H, as a function of γ. Key is the same as in Figure 19.

Plugging Equation (21) into Equation (20), we obtain:

$$\frac{d^2\hat{\phi}_i}{dz^2} - k^2\hat{\phi}_i = 0, \tag{22}$$

which solving for ϕ_i yields $\hat{\phi}_i = A_i \cosh(kz) + B_i \sinh(kz)$. Now assuming that the depth of the upper layer is H_1 and of the lower layer is H_2 and that the interface is at $z = 0$, we apply the 4 boundary conditions to solve for the 4 unknown coefficients. First, at $z = H_1, H_2$

$$\frac{d\hat{\phi}_i}{dz} = 0, \tag{23}$$

such that

$$\frac{d\hat{\phi}_1}{dz} = kA_1 \sinh(H_1 k) + kB_1 \cosh(H_1 k) = 0, \tag{24}$$

and

$$\frac{d\hat{\phi}_2}{dz} = kA_2 \sinh(-H_2 k) + kB_2 \cosh(-H_2 k) = 0. \tag{25}$$

Next, at the interface ($z = 0$), it must hold that

$$\frac{d\hat{\phi}_1}{dz} = \frac{d\hat{\phi}_2}{dz}, \tag{26}$$

such that

$$kA_1 \sinh(0) + kB_1 \cosh(0) = kA_2 \sinh(0) + kB_2 \cosh(0),$$

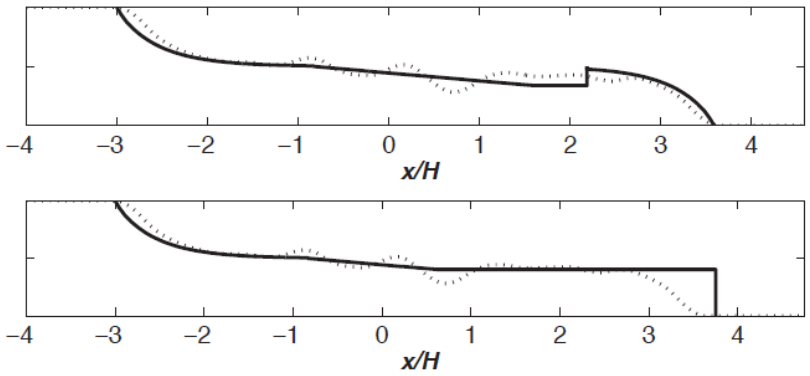

Figure 21: Theoretical interface shape (solid line) compared with computed shape (dotted line) from simulations with the top figure using theory with a bore (energy-preserving heavy gravity current), and the bottom figure using theory without a bore (dissipative heavy current).

yielding

$$B_1 = B_2. \tag{27}$$

Finally, the pressure at the interface also must be equal. In this case, the pressure is expressed as $p_i = g\rho_i z + \rho_i \frac{\partial \phi_i}{\partial t}$, so if $p_1 = p_2$ at $z = 0$, then

$$\begin{aligned} \rho_1 \hat{\phi_1}(0)(-ikc)e^{ik(x-ct)} &= \rho_2 \hat{\phi_2}(0)(-ikc)e^{ik(x-ct)}, \\ \implies \rho_1 \hat{\phi_1}(0) &= \rho_2 \hat{\phi_2}(0), \\ \implies \frac{\rho_1}{\rho_2} = \gamma &= \frac{\hat{\phi_1}(0)}{\hat{\phi_2}(0)} = \frac{A_1}{A_2}. \end{aligned} \tag{28}$$

Now, forming a linear system with 4 equations and 4 unknowns (A_1, B_1, A_2, B_2), we can find an expression such that the determinant of the coefficient matrix is equal to zero, yielding an expression that relates the wave number k and γ,

$$\tanh(kH_1) + \gamma \tanh(kH_2) = \frac{\gamma}{1-\gamma} \frac{(U_1 - U_2)^2}{g/k}. \tag{29}$$

Figure 22 shows the regions of stability for the light and heavy gravity currents for different γ and k values. The light gravity current has an increasingly greater stability region for smaller γ values, even at a high wave number.

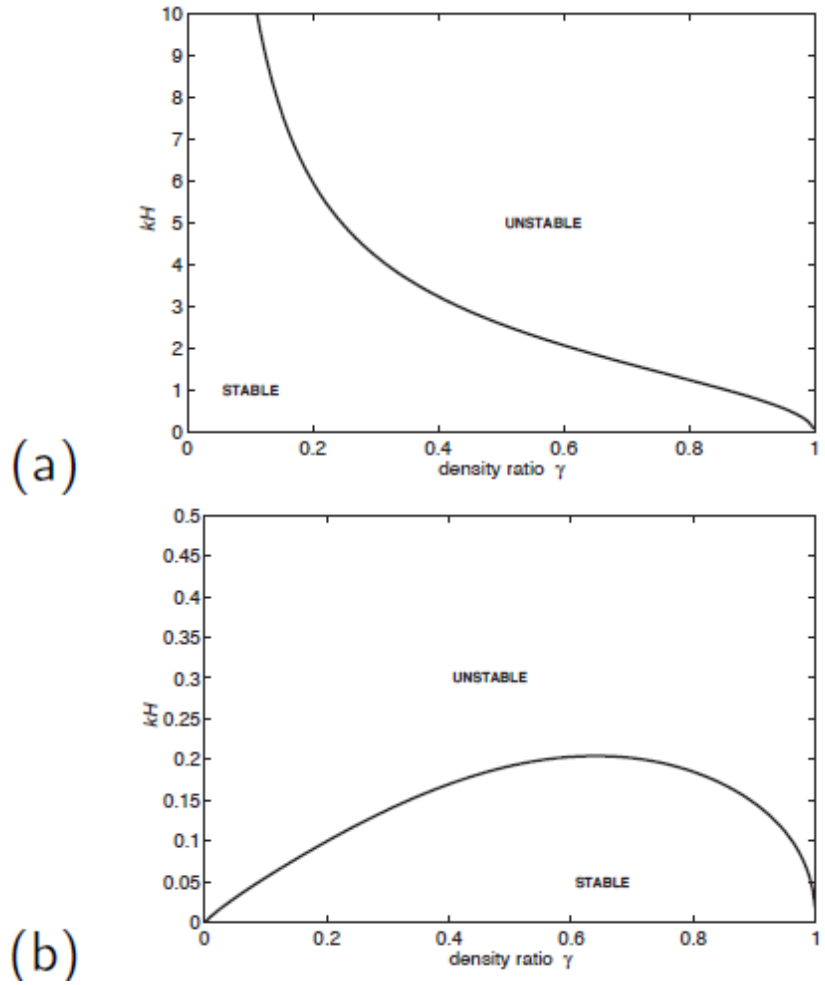

Figure 22: Wavenumber k as a function of γ for which the gravity current interface is neutrally stable according to linear stability theory; (a) light gravity current, (b) heavy gravity current.

References

[1] V. Birman, J.E. Martin, and E. Meiburg, *The non-boussinesq lock exchange problem. part 2. high resolution simulations.*, J. Fluid Mech., 537 (2005), pp. 125–144.

[2] Z Borden and E. H. Meiburg, *Circulation-based models for boussinesq internal bores*, J. Fluid Mech., 726, R1 (2013), pp. 1–11.

[3] J.W.M. Bush and J.M. Aristoff, *The influence of surface tension on the circular hydraulic jump*, J. Fluid Mech., 489 (2003), pp. 229–238.

[4] V. H. Chu and R. E. Baddour, *Surges, waves and mixing in two-layer density stratified flow*, in Proc. 17th Congr. I. A. H. R., vol. 1, 1977, pp. 303–310.

[5] T. Foglizzo, F. Masset, J. Guilet, and G. Durand, *Shallow water analogue of the standing accretion shock instability: Experimental demonstration and an two-dimensional model*, Phys. Rev. Lett., 108 (2012).

[6] H. P. Gröbelbauer, T. K. Fanneløp, and R. E. Britter, *The propagation of intrusion fronts of high density ratios*, J. Fluid Mech., 250 (1993), pp. 669–687.

[7] J. J. Keller and Y.-P. Chyou, *On the hydraulic lock exchange problem*, J. Appl. Math. Phys., 42 (1991), pp. 874–909.

[8] J. B. Klemp, R. Rottuno, and W. C. Skamarock, *On the propagation of internal bores*, J. Fluid Mech., 331 (1997), pp. 81–106.

[9] R. J. Lowe, J. W. Rottman, and P. F. Linden, *The non-Boussinesq lock exchange problem. Part 1. Theory and experiments*, J. Fluid Mech., 537 (2005), pp. 101–124.

[10] J. W. Rottman and J. E. Simpson, *Gravity currents produced by instantaneous release of a heavy fluid in a rectangular channel*, J. Fluid Mech., 135 (1983), pp. 95–110.

[11] J. O. Shin, *Colliding Gravity Currents*, PhD thesis, University of Cambridge, 2002.

[12] R. J. Trapp, *Mesoscale-convective processes in the atmosphere*, Cambridge University Press, 2013.

[13] I. R Wood and J. E. Simpson, *Jumps in layered miscible fluids*, J. Fluid Mech., 140 (1984), pp. 329 – 342.